Bridging spatiotemporal scales of normal fault growth using numerical models of continental extension

Sophie Pan[1], John Naliboff[2], Rebecca Bell[1] and Chris Jackson[3]

[1]Earth Science and Engineering, Imperial College, Prince Consort Road, London, SW7 2BP, UK

[2]Department of Earth and Environmental Science, New Mexico Institute of Mining and Technology, NM, USA

[3]Department of Earth and Environmental Sciences, The University of Manchester, Williamson Building, Oxford Road, Manchester, M13 9PL, UK

ABSTRACT

Continental extension is accommodated by the development of kilometre-scale normal faults, which grow by accumulating metre-scale earthquake slip over millions of years. Reconstructing the entire lifespan of a fault remains challenging due to a lack of observational data of appropriate scale, particularly over intermediate timescales (10^4-10^6 yrs). Using 3D numerical simulations of continental extension and novel automated image processing, we examine key factors controlling the growth of very large faults over their entire lifetime. Modelled faults quantitatively show key geometric and kinematic similarities with natural fault populations, with early faults (i.e., those formed within ca. 100 kyrs of extension) exhibiting scaling ratios consistent with those characterising individual earthquake ruptures on active faults.

Our models also show that while finite lengths are rapidly established (< 100 kyrs), active deformation is highly transient, migrating both along- and across-strike. Competing stress interactions determine the overall distribution of active strain, which oscillates locally between localised and continuous slip, to distributed and segmented slip. These findings demonstrate that our understanding of fault growth and the related occurrence of earthquakes is more complex than that currently inferred from observing finite displacement patterns on now-inactive structures, which only provide a spatial- and time-averaged picture of fault kinematics and related geohazard.

INTRODUCTION

Recent advancements in geodetic measurements allow for high-resolution surface observations of crustal deformation (e.g., Elliott et al., 2016). Seismological and geodetic data from a particular earthquake are inverted using modelled fault geometry to infer slip distribution and magnitude (e.g., Wilkinson et al., 2015; Walters et al., 2018). These data show that individual earthquake rupture patterns are variable and complex, with events typically temporally and spatially clustered (e.g., Coppersmith, 1989; Nicol et al., 2006). Rupture lengths are often considerably shorter than finite fault lengths, and multiple segment ruptures during a single event can trigger surprisingly high-magnitude, hazardous earthquakes (7.9 M_w Kaikoura, New Zealand; Hamling et al., 2017; 7.2 M_w El Mayor-Cucapah, Mexico; Fletcher et al., 2014) that have recently challenged seismic hazard assessments (Field et al., 2014).

Large (e.g., tens of kilometres long, several kilometres of displacement) normal faults grow by accumulating m-scale slip during earthquakes. In contrast to the short-time complexity captured by seismological and geodetic data, 3D seismic reflection and field data show that slip rates can be stable over substantially longer timescales (i.e., $>10^6$ yrs), incorporating potentially thousands of seismic cycles distributed over millions of years. These data reveal that fault displacement (i.e., cumulative slip) may simultaneously increase with length (the 'propagating' model; Walsh and Watterson, 1988), or accumulate on faults of near-constant length (the 'constant-length' model; Walsh et al., 2002; Rotevatn et al., 2019; Pan et al., 2021). It is challenging to reconstruct fault growth over shorter timescales ($<10^6$ yrs) using these data, principally due to: (i) limited seismic reflection data resolution in the subsurface; (ii) the lack of exposures of hangingwall growth strata in the field; and (iii) a lack of age-constraints on syn-kinematic (growth) strata in both subsurface and field (Jackson et al., 2017).

Due to the lack of observational datasets of the appropriate temporal and spatial scale, it remains unclear how the short-term variability of earthquake slip eventually results in stable, long-term displacement accumulation across large, mature faults. Slip rates measured from geodetic measurements such as Interferometric Synthetic Aperture Radar (InSAR) and Global Navigation Satellite System (GNSS) are often used to infer their geological rates (e.g., Wallace et al., 2009), but the former often appear systematically higher than the latter (Dixon et al., 2003; Oskin 2007; Bell et al., 2011). Bridging the spatiotemporal gaps, particularly over intermediate timescales (10^4-10^6 yrs), is therefore critical, given this can provide key first-order controls on slip geometry (Nicol et al., 2005, 2006), improving our ability to forecast the location and magnitude of potentially hazardous earthquakes (Roberts and Michetti, 2004).

Here, we use high-resolution (<650 m) thermal-mechanical 3D simulations of continental extension to examine the evolution of normal fault networks across spatiotemporal scales poorly sampled by observational datasets. Using novel image processing techniques, the active length, strain and cumulative strain are extracted from large fault populations across multiple timesteps and compared to natural D-L observations, providing insights into the kinematics that constrain fault growth, and the underlying dynamics that govern their evolution.

NUMERICAL APPROACH

The models span 500 (width) x 500 (length) x 100 (depth) km and contain distinct thermodynamic and rheological properties for the upper crust, lower crust and mantle, which deform through a combination of non-linear viscous and plastic brittle deformation. The velocity constraints, initial strength and temperature profile and compositional material properties closely follow Naliboff et al. (2020). We test the effects of three extension rates; 2.5, 5 and 10 mm yr^{-1} (Fig. 1). To achieve sufficiently high numerical resolutions within the fault network, successive spatially-defined adaptive refinement increases the resolution from 5000 m to 625 m over a centered 180 x 180 x 20 km region (Supplementary Fig. 1), from which we extract the fault population. Broadly, this approach provides 'natural' boundary conditions for distributed fault networks within the upper crust.

In contrast to Naliboff et al. (2020), we apply a new approach that partitions initial heterogeneity into a randomised, binary distribution consisting of 5 km^3 strong and weak blocks. This promotes the significantly faster formation of complex, discrete fault populations (Fig. 1). From a geological perspective, this form of random but pervasive damage may reflect structural inheritance observed in natural systems, where deformation exploits inherited weaknesses such as pre-existing faults (e.g., Phillips et al., 2016) or the margins of strong zones (e.g., ancient cratons; e.g., Dunbar and Sawyer, 1989).

The 3D model results are analysed on a horizontal plane located 5 km below the initial model surface. To quantitatively analyse the geometry and kinematics of faults, fault identification and extraction is required (Fig. 1). We employ a Python workflow based on the spatial vertical derivative of the active deformation field (Supplementary Fig. 2), which effectively extracts localised, clustered regions of strain (i.e., relatively steep gradients of strain-profiles). This novel approach successfully recovers detailed interactions between distinct active fault strands without manual input across multiple timesteps. See the Supplemental Material for full details of our forward modelling and fault extraction approach.

MODELS PRODUCE REALISTIC FAULT PATTERNS

Our model results show that in the final stages of rifting, the strain rate magnitude (Fig. 1A-C) and extracted active fault locations (Fig. 1D-F) for models with extension rates of 2.5, 5, or 10 mm yr^{-1} reveal active deformation accommodated along complex fault networks. In models with faster extension rates, the overall magnitude of strain rate increases and is accommodated across increasingly diffuse zones of deformation (Fig. 1A-C). These networks contain faults of varying lengths (c. 5-120 km), which often contain along-strike changes in strike, and that may splay and link with adjacent structures. This complexity reflects both the randomisation of the initial plastic strain field and the mechanical and kinematic interaction between adjacent faults.

Overall, the fault network is geometrically similar, based on displacement-length (D-L) scaling relationships, to those identified in natural systems (Fig. 2) (e.g., Walsh and Watterson, 1991).

FAULT PATTERNS ARE RAPIDLY ESTABLISHED

During the earliest stages of rifting, i.e., within the first resolvable timestep (c. 200, 100 and 50 kyrs for extension rates of 2.5, 5, or 10 mm yr^{-1}, respectively), active deformation is accommodated along distributed fault networks (Supplementary Video 1, 2) that are similar in appearance to their finite fault patterns (Fig. 1). During the earliest timestep (< 100 kyrs) the faults are seemingly under-displaced compared to geological D-L datasets, instead plotting close to the slip-length ratio associated with individual earthquakes (c = 0.00005; see Wells and Coppersmith, 1994 and Fig. 2A).

As near-maximum finite fault lengths are established from the onset of extension, faults therefore predominantly accumulate displacement and move upwards in D-L space, behaviour consistent with the constant-length fault growth model (e.g., Walsh et al., 2002; Rotevatn et al., 2019; Pan et al., 2021). Our results show that fault lengths are established an order of magnitude (<100 kyrs) earlier than currently inferred from seismic reflection analysis of ancient (c. 1.3 Myrs, NW Shelf, Australian; Walsh et al., 2002) and active (c. 700 kyrs, Whakatane Graben, New Zealand; Taylor et al., 2004) rifts. This rapid establishment of fault patterns suggest fault array growth is kinematically coherent (i.e., faults are part of a larger structure; Walsh and Watterson, 1991; Nicol et al., 2006) from the onset of extension. However, during early extension, all faults are blind and are not topography expressed at the model surface, therefore while lengths rapidly propagated laterally at depth, they may not have propagated vertically into the structural level of observation. This is important, given it is deformation of the Earth's surface, and resulting thickness and facies changes in associated growth strata, that are typically used to constrain normal fault kinematics (Jackson et al., 2017). The stratigraphic record may therefore not record the earliest phase of extension leading to an erroneous assessment of existing fault growth models and the timing of rift initiation and duration.

STRAIN ACCUMULATION REVEALS TRANSIENT BEHAVIOUR

Distinguishing between currently debated fault growth models has direct implications for the nature of earthquake slip and potential moment magnitude, i.e., the 'propagating' model is said to require a progressive temporal increase in the maximum earthquake magnitude, whereas the constant-length model may be associated with constant slip rates and invariant earthquake magnitude and recurrence (Nicol et al., 2005). Whereas our results demonstrate that finite lengths were rapidly established (i.e., 'constant-length' model), they do not explicitly support either of the two slip models, instead showing that active deformation is temporally and spatially variable (i.e., earthquake slip is variable, not uniform), an observation consistent with slip patterns characterising active fault networks (e.g., Friedrich et al., 2003; Oskin et al., 2007) and analogue models (e.g., Schlagenhauf, 2008)

Time-series of the total number of active faults (Fig. 2B) and the average fault length in a given population (Fig. 2C) reveal significant fluctuations throughout time. All three models (with extensions rates of 2.5, 5, 10 mm yr^{-1}) initiate with an increase in fault number and average fault length (Fig. 2B, C), corresponding to an initially diffuse distributed pattern from the first timestep that rapidly localises (i.e., reduces in deformation width) within the first c. 10 timesteps (see Supplementary Videos 1-2, 4-6). Both fault number and mean length continue to fluctuate throughout the remainder of extension, reflecting oscillations between localised and distributed active deformation throughout the crust (Fig 2B, C). This behaviour is consistent with spatiotemporal clustering of earthquakes promoted by stress interactions between neighbouring faults (Stein 1999). Although transient behaviour continues for the remainder of extension, the overall number of faults slowly decreases, and the average fault length slightly increases (Fig 2B, C), demonstrating that large-scale localisation occurs as strain is concentrated onto fewer, larger fault systems (e.g., Cowie, 1998).

Transient deformation occurs both along- and perpendicular to strike, which we view in a regional model subset (Supplementary Video 4-6). Along-strike migration of deformation, which we observe by summing longitudinally across the regional subset (Supplementary Video 7), is consistent with the preferential propagation direction of rupture. The across-strike strain migration correlates to along-strike bends, supporting observations from active settings that earthquakes occur at segment boundaries (DuRoss et al., 2016), and that relays may be associated with throw rate enhancements (Faure-Walker et al., 2009; Iezzi et al., 2018). Overall, along- and across- strain migration, reflective of competing stress-interactions between faults in the near field (e.g., Cowie, 1998) as documented in Fig. 2B and C, produce end-member behaviours characterised by localised, continuous slip (Fig. 3A-C) and distributed, segmented slip (Fig. 3D-F). This transient behaviour evolves without explicitly modelling the earthquake cycle via a rate or rate-state friction type rheology (e.g., Dinther et al., 2013), suggesting that the recurrence of large, clustered slip (e.g., Fig. 3A) can be mechanically underpinned by far-field, dynamic triggering i.e., constant rates of tectonic extension.

The short-term variability and long-term stability of strain accumulation on the modelled fault networks may be reconciled by considering how deformation is aggregated, both spatially and temporally. As deformation is longitudinally summed across (latitudinally) increasing regions, the strain rate profile becomes increasingly uniform as strain deficits in one location is compensated for by increased strain in other, across-strike locations (Supplementary Video 7). This reflects the coherence of faults at spatial scales larger than the individual fault surface (e.g., Nicol et al., 2006). Small-scale, distributed deformation in the form of near-fault drag accounted for 30% greater geodetic slip rates (Oskin 2007). We suspect this value could be higher if the spatial scale of observation increases to accommodate all distributed deformation, particularly at higher extension rates (10 mm yr^{-1}) where distributed deformation is relatively widespread (e.g., Fig. 1). Furthermore, if geodetic rates are more likely to be measured from clustered earthquake slip (i.e., Fig. 3A-C), this may likely transiently exceed the geological slip average, given that interseismic periods of diffuse deformation (i.e., Fig. 3D-F) are less likely to be recorded, if deformation is expressed at all.

These findings demonstrate that fault network evolution is more complex than currently inferred from observing finite displacement patterns on now-inactive structures (i.e., finite strain in Fig 3B and 3E appear nearly identical), which provide only a time-averaged picture of fault kinematics. Subsequently, geodetic rates will not necessarily mirror geological rates, as it may only capture a transient snapshot. Conventional D-L profiles may therefore provide only a limited understanding of fault growth, given they do not capture stress- and -time dependent stress interactions crucial to revealing the short- to intermediate-timescale variations in faulting that control earthquake magnitude and location.

ACKNOWLEDGMENTS

PhD work is funded by Natural Environment Research Council (NERC) Centre for Doctoral Training (CDT) in Oil and Gas (NE/R01051X/1). The computational time for these simulations was provided under XSEDE project EAR180001.

REFERENCES CITED

1. Bell, R.E., McNeill, L.C., Henstock, T.J. and Bull, J.M., 2011. Comparing extension on multiple time and depth scales in the Corinth Rift, Central Greece. *Geophysical Journal International*, *186*(2), pp.463-470.
2. Coppersmith, K.J. and Youngs, R.R., 1989. Issues regarding earthquake source characterization and seismic hazard analysis within passive margins and stable continental interiors. In *Earthquakes at North-Atlantic Passive Margins: Neotectonics and Postglacial Rebound* (pp. 601-631). Springer, Dordrecht.
3. Cowie, P.A., 1998. A healing–reloading feedback control on the growth rate of seismogenic faults. *Journal of Structural Geology*, *20*(8), pp.1075-1087.
4. Dawers, N.H. and Underhill, J.R., 2000. The role of fault interaction and linkage in controlling synrift stratigraphic sequences: Late Jurassic, Statfjord East area, northern North Sea. *AAPG bulletin*, *84*(1), pp.45-64.

5. Dixon, T.H., Norabuena, E. and Hotaling, L., 2003. Paleoseismology and Global Positioning System: Earthquake-cycle effects and geodetic versus geologic fault slip rates in the Eastern California shear zone. *Geology*, *31*(1), pp.55-58.
6. Duclaux, G., Huismans, R.S. and May, D.A., 2020. Rotation, narrowing, and preferential reactivation of brittle structures during oblique rifting. *Earth and Planetary Science Letters*, *531*, p.115952.
7. Dunbar, J.A. and Sawyer, D.S., 1989. How preexisting weaknesses control the style of continental breakup. *Journal of Geophysical Research: Solid Earth*, *94*(B6), pp.7278-7292.
8. DuRoss, C.B., Personius, S.F., Crone, A.J., Olig, S.S., Hylland, M.D., Lund, W.R. and Schwartz, D.P., 2016. Fault segmentation: New concepts from the Wasatch fault zone, Utah, USA. *Journal of Geophysical Research: Solid Earth*, *121*(2), pp.1131-1157.
9. Elliott, J.R., Walters, R.J. and Wright, T.J., 2016. The role of space-based observation in understanding and responding to active tectonics and earthquakes. *Nature communications*, *7*(1), pp.1-16.
10. Field, E.H., Arrowsmith, R.J., Biasi, G.P., Bird, P., Dawson, T.E., Felzer, K.R., Jackson, D.D., Johnson, K.M., Jordan, T.H., Madden, C. and Michael, A.J., 2014. Uniform California earthquake rupture forecast, version 3 (UCERF3)—The time-independent model. *Bulletin of the Seismological Society of America*, *104*(3), pp.1122-1180.
11. Fletcher, J.M., Teran, O.J., Rockwell, T.K., Oskin, M.E., Hudnut, K.W., Mueller, K.J., Spelz, R.M., Akciz, S.O., Masana, E., Faneros, G. and Fielding, E.J., 2014. Assembly of a large earthquake from a complex fault system: Surface rupture kinematics of the 4 April 2010 El Mayor–Cucapah (Mexico) Mw 7.2 earthquake. *Geosphere*, *10*(4), pp.797-827.

12. Friedrich, A.M., Wernicke, B.P., Niemi, N.A., Bennett, R.A. and Davis, J.L., 2003. Comparison of geodetic and geologic data from the Wasatch region, Utah, and implications for the spectral character of Earth deformation at periods of 10 to 10 million years. *Journal of Geophysical Research: Solid Earth*, *108*(B4).

13. Hamling, I.J., Hreinsdóttir, S., Clark, K., Elliott, J., Liang, C., Fielding, E., Litchfield, N., Villamor, P., Wallace, L., Wright, T.J. and D'Anastasio, E., 2017. Complex multifault rupture during the 2016 Mw 7.8 Kaikōura earthquake, New Zealand. *Science*, *356*(6334).

14. Iezzi, F., Mildon, Z., Walker, J.F., Roberts, G., Goodall, H., Wilkinson, M. and Robertson, J., 2018. Coseismic throw variation across along-strike bends on active normal faults: Implications for displacement versus length scaling of earthquake ruptures. *Journal of Geophysical Research: Solid Earth*, *123*(11), pp.9817-9841.

15. Jackson, C.A.L., Bell, R.E., Rotevatn, A. and Tvedt, A.B., 2017. Techniques to determine the kinematics of synsedimentary normal faults and implications for fault growth models. *Geological Society, London, Special Publications*, *439*(1), pp.187-217.

16. Naliboff, J.B., Glerum, A., Brune, S., Péron-Pinvidic, G. and Wrona, T., 2020. Development of 3-D rift heterogeneity through fault network evolution. *Geophysical Research Letters*, *47*(13), p.e2019GL086611.

17. Nicol, A., Walsh, J., Berryman, K. and Villamor, P., 2006. Interdependence of fault displacement rates and paleoearthquakes in an active rift. *Geology*, *34*(10), pp.865-868.

18. Nicol, A., Walsh, J.J., Manzocchi, T. and Morewood, N., 2005. Displacement rates and average earthquake recurrence intervals on normal faults. *Journal of Structural Geology*, *27*(3), pp.541-551.

19. Oskin, M., Perg, L., Blumentritt, D., Mukhopadhyay, S. and Iriondo, A., 2007. Slip rate of the Calico fault: Implications for geologic versus geodetic rate discrepancy in the Eastern California Shear Zone. *Journal of Geophysical Research: Solid Earth*, *112*(B3).

20. Phillips, T.B., Jackson, C.A., Bell, R.E., Duffy, O.B. and Fossen, H., 2016. Reactivation of intrabasement structures during rifting: A case study from offshore southern Norway. *Journal of Structural Geology*, *91*, pp.54-73.

21. Roberts, G.P. and Michetti, A.M., 2004. Spatial and temporal variations in growth rates along active normal fault systems: an example from The Lazio–Abruzzo Apennines, central Italy. *Journal of Structural Geology*, *26*(2), pp.339-376.

22. Roberts, G.P. and Michetti, A.M., 2004. Spatial and temporal variations in growth rates along active normal fault systems: an example from The Lazio–Abruzzo Apennines, central Italy. *Journal of Structural Geology*, *26*(2), pp.339-376.

23. Rotevatn, A., Jackson, C.A.L., Tvedt, A.B., Bell, R.E. and Blækkan, I., 2019. How do normal faults grow?. *Journal of Structural Geology*, *125*, pp.174-184.

24. Schlagenhauf, A., Manighetti, I., Malavieille, J. and Dominguez, S., 2008. Incremental growth of normal faults: Insights from a laser-equipped analog experiment. *Earth and Planetary Science Letters*, *273*(3-4), pp.299-311.

25. Stein, R.S., 1999. The role of stress transfer in earthquake occurrence. *Nature*, *402*(6762), pp.605-609.

26. Taylor, S.K., Bull, J.M., Lamarche, G. and Barnes, P.M., 2004. Normal fault growth and linkage in the Whakatane Graben, New Zealand, during the last 1.3 Myr. *Journal of Geophysical Research: Solid Earth*, *109*(B2)

27. Van Dinther, Y., Gerya, T.V., Dalguer, L.A., Corbi, F., Funiciello, F. and Mai, P.M., 2013. The seismic cycle at subduction thrusts: 2. Dynamic implications of geodynamic simulations validated with laboratory models. *Journal of Geophysical Research: Solid Earth*, *118*(4), pp.1502-1525.

28. Walker, J.F., Roberts, G.P., Cowie, P.A., Papanikolaou, I.D., Sammonds, P.R., Michetti, A.M. and Phillips, R.J., 2009. Horizontal strain-rates and throw-rates across breached relay zones, central Italy: Implications for the preservation of throw deficits at points of normal fault linkage. *Journal of Structural Geology*, *31*(10), pp.1145-1160.

29. Wallace, L.M., Ellis, S., Miyao, K., Miura, S., Beavan, J. and Goto, J., 2009. Enigmatic, highly active left-lateral shear zone in southwest Japan explained by aseismic ridge collision. *Geology*, *37*(2), pp.143-146.

30. Walsh, J.J. and Watterson, J., 1988. Analysis of the relationship between displacements and dimensions of faults. *Journal of Structural geology*, *10*(3), pp.239-247.

31. Walsh, J.J., Nicol, A. and Childs, C., 2002. An alternative model for the growth of faults. *Journal of Structural Geology*, *24*(11), pp.1669-1675.

32. Walters, R.J., Gregory, L.C., Wedmore, L.N., Craig, T.J., McCaffrey, K., Wilkinson, M., Chen, J., Li, Z., Elliott, J.R., Goodall, H. and Iezzi, F., 2018. Dual control of fault intersections on stop-start rupture in the 2016 Central Italy seismic sequence. *Earth and Planetary Science Letters*, *500*, pp.1-14.

33. Wells, D.L. and Coppersmith, K.J., 1994. New empirical relationships among magnitude, rupture length, rupture width, rupture area, and surface displacement. *Bulletin of the seismological Society of America*, *84*(4), pp.974-1002.

34. Wilkinson, M., Roberts, G.P., McCaffrey, K., Cowie, P.A., Walker, J.P.F., Papanikolaou, I., Phillips, R.J., Michetti, A.M., Vittori, E., Gregory, L. and Wedmore, L., 2015. Slip distributions on active normal faults measured from LiDAR and field mapping of geomorphic offsets: an example from L'Aquila, Italy, and implications for modelling seismic moment release. *Geomorphology*, *237*, pp.130-141.

FIGURE CAPTIONS

Figure 1. The top row shows the strain rate invariant (s^{-1}) in the upper crust (5 km depth), documenting active deformation patterns within the last resolvable time increment for models ran at 2.5, 5, and 10 mm yr^{-1} respectively. The bottom row shows their corresponding fault length extracted from the active deformation field.

Figure 2. Geometric statistics of time-dependent fault properties. **A)** Fault D-L evolution for the modelled fault network that experienced 5 mm yr^{-1} extension. Observational datasets are plotted in grey, where different shades correlate to references therein. **B)** The number of active faults throughout time. **C)** The average active length of the network throughout time. Note that all three models output 50 timesteps, however the age duration for models deformed at 2.5, 5 and 10 mm yr^{-1} are 10, 5 and 2.5 Myrs, respectively.

Figure 3. End-member behaviour of transient deformation. Along-strike map of a subset of the model that experienced 10 mm yr^{-1} extension. The strain rate invariant **(A)**, finite strain **(B)**, and extracted faults **(C)** at 2.1 Myrs reveal localised behaviour. The strain rate **(D)**, finite strain **(E)** and extracted faults **(F)** at 2.2 Myrs reveal distributed behaviour.

[1] GSA Data Repository item 2021, containing detailed methods of the forward modelling and fault extraction with reproducible datasets, is available online at www.geosociety.org/pubs/ft20XX.htm, or on request from editing@geosociety.org.

Figure 1. The top row shows the strain rate invariant (s^{-1}) in the upper crust (5 km depth), documenting active deformation patterns within the last resolvable time increment (10, 5 and 2.5 Myrs for models ran at 2.5, 5, and 10 mm yr^{-1} respectively). The bottom row shows their corresponding fault length property extracted from the active deformation field. The spatial extent covers the high-resolution (625 m) portion of the model domain.

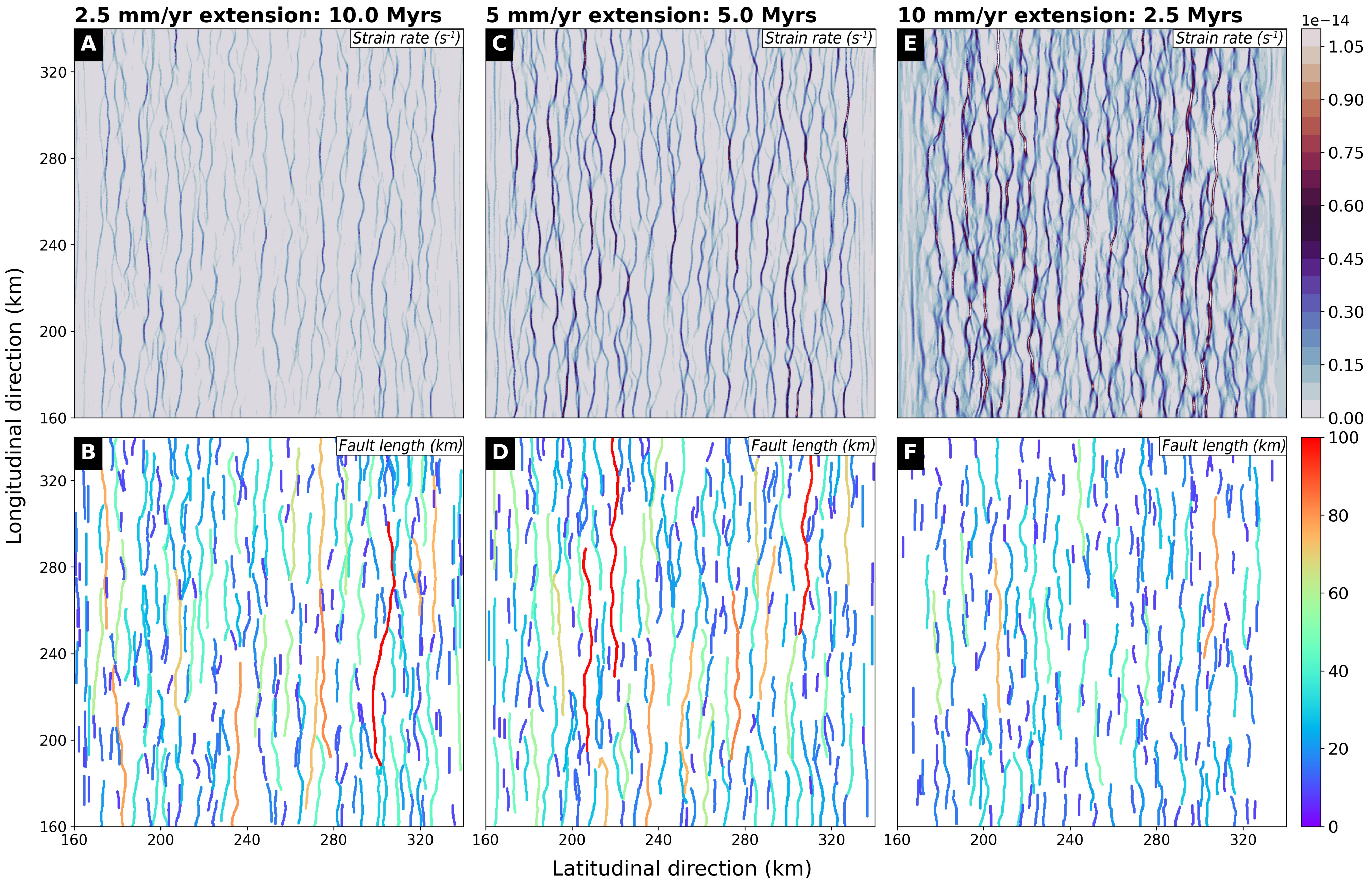

Figure 2. Geometric statistics of time-dependent fault properties. **A)** Fault D-L evolution for the modelled fault network that experienced 5 mm yr^{-1} extension. D-L geometries of observable faults are plotted in grey, where different shades correlate to different datasets (references therein). **B)** The number of active faults throughout model evolution all models. **C)** The average active length of a given population throughout model evolution. Note that all three models output 50 timesteps, however the age duration for models deformed at 2.5 mm yr^{-1}, 5 mm yr^{-1} and 10 mm yr^{-1} are 10 Myrs, 5 Myrs and 2.5 Myrs respectively.

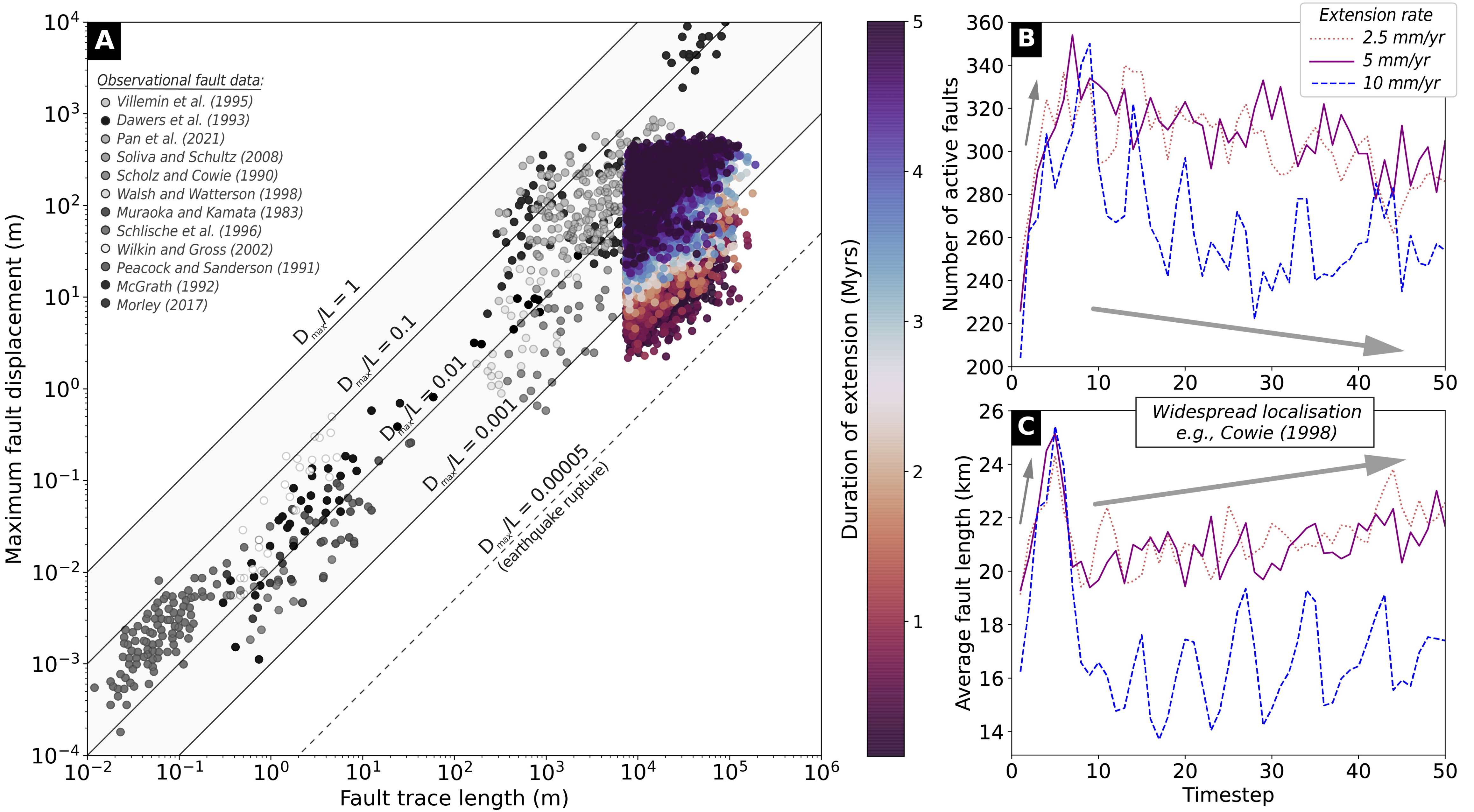

Figure 3. End-member behaviour of transient deformation. Along-strike map of a subset of the model that experienced 10 mm yr^{-1} extension. The strain rate invariant **(A)**, finite strain **(B)**, and extracted faults **(C)** at 2.1 Myrs reveal localised behaviour. The strain rate **(D)**, finite strain **(E)** and extracted faults **(F)** at 2.2 Myrs reveal distributed behaviour.

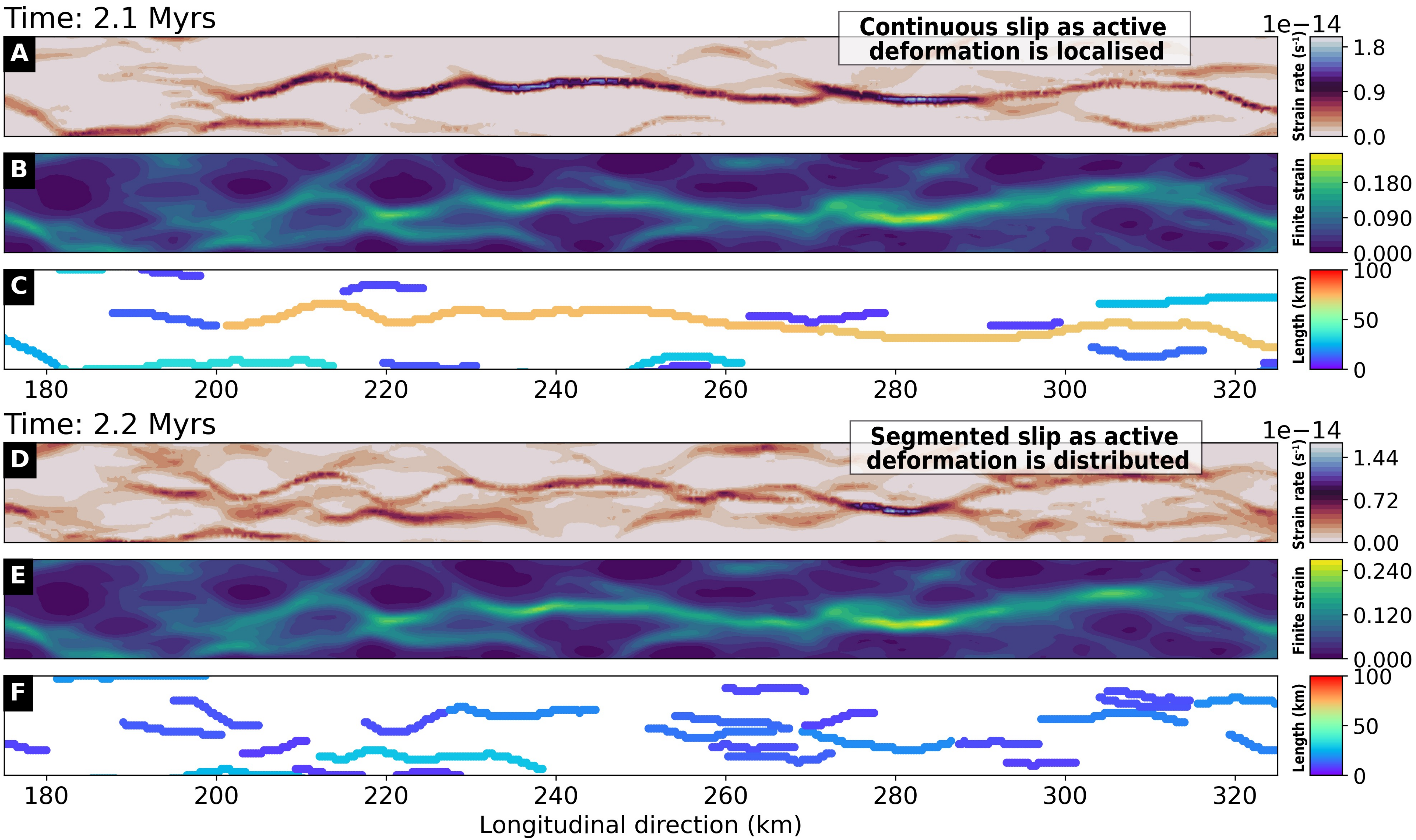

GSA DATA REPOSITORY **Pan, Naliboff, Bell and Jackson**

SUPPLEMENTARY MATERIAL

Numerical Simulations

Model Geometry and Resolution

The governing equations are solved on a 3D gridded domain which spans 500 by 500 km across the horizontal plane (X, Y) and 100 km in the depth (Z) direction. The grids are coarsest (5 km) on the sides and base of the model domain and are successively reduced using adaptive-mesh refinement, increasing the resolution to 625 m over a centered 180 x 180 x 20 km region (Supplementary Fig. 1). Throughout the model domain we use quadratic elements (Equation 2) elements to solve the advection-diffusion equation for temperature and composition, while the Stokes equation is solved on elements that are quadratic for velocity and continuous linear for pressure (Equations 1 and 2).

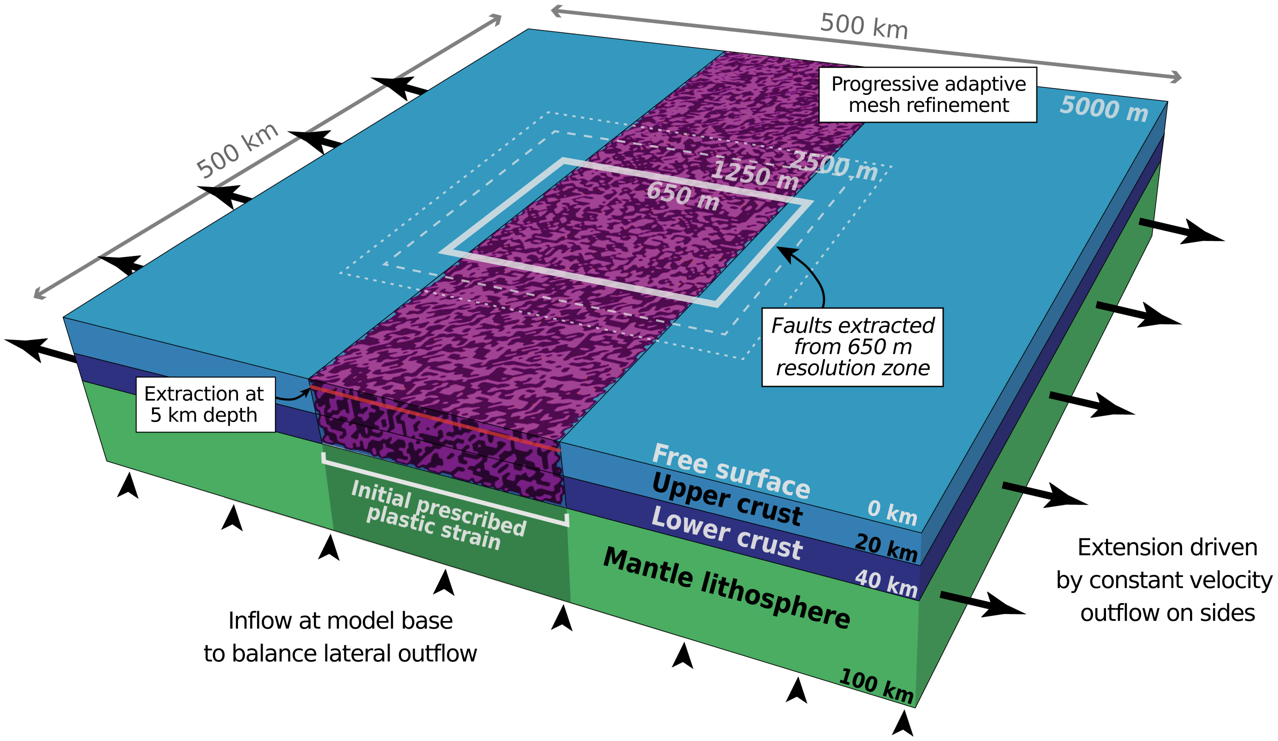

Supplemental Figure 1. 3D model setup outlining initial boundary conditions, compositional layers and prescribed initial strain. Resolution is progressively refined to higher levels up to 650 in the centre, where we perform fault extraction at 5 km depth.

Governing equations

We use the open-source, mantle convection and lithospheric dynamics code ASPECT (Kronbichler et al., 2012; Heister et al., 2017) to model 3D continental extension following the approach of Naliboff et al. (2020). The model solves the incompressible Boussinesq approximation of momentum, mass and energy equations, combined with advection-diffusion equations which are outlined below. The Stokes equation which solves for velocity and pressure are defined as:

$$\nabla \cdot \boldsymbol{u} = 0 \tag{1}$$

$$-\nabla \cdot 2\,\mu\,\dot{\varepsilon}(\boldsymbol{u}) + \nabla p = \rho \boldsymbol{g} \tag{2}$$

Where $\boldsymbol{u}$ is the velocity, μ is the viscosity, $\dot{\varepsilon}$ is the second deviator of the strain rate tensor, p is pressure, ρ is density, and $\boldsymbol{g}$ is gravitational acceleration.

Temperature evolves through a combination of advection, heat conduction, shear heating, and adiabatic heating:

$$\rho C_p \left(\frac{\partial T}{\partial t} + \boldsymbol{u} \cdot \nabla T\right) - \nabla \cdot \left(\kappa \rho C_p\right) \nabla T = \rho H + 2\eta\,\dot{\varepsilon}(\boldsymbol{u}) + \alpha T\,(\boldsymbol{u} \cdot \nabla p) \tag{3}$$

Where C_p is the heat capacity, T is temperature, t is time, κ is thermal diffusivity, and H is the rate of internal heating. Respectively, the terms on the right-hand side correspond to internal head production, shear heating, and adiabatic heating.

Density varies linearly as a function of the reference density (ρ_0), thermal expansivity (α), reference temperature (T_0) and temperature:

$$\rho = \rho_0 \left(1 - \alpha\,(T - T_0)\right) \tag{4}$$

Rheological Formulation

Rheological behaviour combines nonlinear viscous flow with brittle failure (see Glerum et al., 2018). Viscous flow follows dislocation creep, formulated as:

$$\sigma'_{II} = A^{-\frac{1}{n}} \dot{\varepsilon}_{II}^{\frac{1}{n}} e^{\frac{Q+P\,V}{n\,R\,T}} \tag{5}$$

Above, σ'_{II} is the second invariant of the deviatoric stress, A is the viscous prefactor, n is the stress exponent, $\dot{\varepsilon}_{II}$ is the second invariant of the deviatoric strain rate (effective strain rate), Q is the activation energy, P is pressure, V is the activation volume, T is temperature, and R is the gas constant

Brittle plastic deformation follows a Drucker Prager yield criterion, which accounts for softening of the angle of internal friction (ϕ) and cohesion (C) as a function of accumulated plastic strain:

$$\sigma'_{II} = \frac{6\,C\ \cos\phi + \ 2\,P\ \sin\phi}{\sqrt{(3)}(3\ +\ \sin\phi)} \tag{6}$$

The initial friction angle and cohesion are 30 and 20 MPa respectively, and linearly weaken by a factor of 2 as a function of finite plastic strain. We localise deformation in the center of the model by prescribing an initial plastic strain field. Rather than a single weak seed (e.g., Lavier et al., 2000; Thieulot, 2011; Huismans et al., 2007), or randomised distribution (e.g., Naliboff et al., 2017; Naliboff et al., 2020; Duclaux et al., 2020), the initial plastic strain field is partitioned into 5 km coarse blocks which are randomly assigned 0.5 or 1.5. This method results in statistically random but pervasive damage using an adjustable wavelength (i.e., the block size) which allows for the adjustment of spatial distribution without changing the overall initial damage/strain. The data file (composition.txt) containing the initial distribution of plastic strain and additional compositional field data, as well as the python script to generate this data (composition.py) are located in the supplementary data set.

The viscosity is calculated using the viscosity rescaling method, where if the viscous stress exceeds plastic yield stress, the viscosity is reduced such that the effective stress matches the plastic yield (see Glerum et al., 2018). Nonlinearities from the Stokes equations are addressed by applying defect-Picard iterations (Fraters et al., 2019) to a tolerance of 1e^{-4}. The maximum numerical time step is limited to 20 kyr.

Initial Conditions

The model domain contains three distinct compositional layers, representing the upper crust (0-20 km depth), lower crust (20-40 km depth), and lithospheric mantle (40-100 km depth). Distinct background densities (2700, 2800, 3300 kg m^{-3}) and viscous flow laws for dislocation creep (wet quartzite (Gleason and Tullis, 1995), wet anorthite (Rybacki et al., 2003), dry olive (Hirth and Kohlstedt, 2003) distinguish these three layers, which deform through a combination of nonlinear viscous flow and brittle (plastic) deformation (Glerum et al., 2018; Naliboff et al., 2020). Supplementary Table 1 contains the specific parameters for each flow law.

The initial temperature distribution follows a characteristic conductive geotherm for the continental lithosphere (Chapman, 1986). We solve for the conductive profile by first assuming a thermal conductivity of 2.5 W m^{-1} K^{-1}, a surface temperature of 273 K, and a surface heat flow of 55 mW/m2, and constant radiogenic heating in each compositional layer (Supplementary Table 1) which we use to calculate the temperature with depth within each layer. The resulting temperature at the base of the upper crust, lower crust, and mantle lithosphere, respectively, are 633, 893, and 1613 ^{o}K. Supplementary file (geotherm.py) provides an example of how to calculate the geothermal profile and extract the parameters required to reproduce this initial profile within the ASPECT parameter file.

Supplementary Table 1. Material properties for distinct compositional layers

Compositional layer	**Upper crust**	**Lower crust**	**Mantle lithosphere**
Reference density	2700 kg m^{-3}	2900 kg m^{-3}	3250 kg m^{-3}
Viscosity prefactor (A*)	8.57 x 10^{-28} Pa^{-n} m^{-p} s^{-1}	7.13 x 10^{-18} Pa^{-n} m^{-p} s^{-1}	6.52 x 10^{-16} Pa^{-n} m^{-p} s^{-1}
n	4	3	3.5
Activation energy (Q)	223 kJ mol^{-1}	345 kJ mol^{-1}	530 kJ mol^{-1}
Activation volume (V)	N/A	N/A	18 x 10^{6} m^{3} mol^{-1}
Specific heat (C_p)	750 J kg^{-1} k^{-1}	750 J kg^{-1} k^{-1}	750 J kg^{-1} k^{-1}
Thermal conductivity (K)	2.5 W m^{-1} K^{-1}	2.5 W m^{-1} K^{-1}	2.5 W m^{-1} K^{-1}
Thermal expansivity (A)	2.5 x 10^{-5} K^{-1}	2.5 x 10^{-5} K^{-1}	2.5 x 10^{-5} K^{-1}
Heat production (H)	1 x 10^{-6} W m^{-3}	0.25 x 10^{-6} W m^{-3}	0
Friction angle (ϕ)	30 °	30 °	30 °
Cohesion angle (C)	20 MPa	20 MPa	20 MPa

Boundary Conditions

Deformation is driven by prescribed outflow velocities on the left and right sides (i.e., orthogonal extension), with inflow at the model base exactly balancing the outflow. The top of the model is a free surface (Rose et al., 2015) and is advected normal to the velocity field. The extension rate (i.e., the prescribed outward velocity) is 2.5, 5 and 10 mm/yr (Fig. 1).

Compiling and Running ASPECT

The model in this study were run with ASPECT version 2.2.0-pre at commit ab5eead39. This version of ASPECT can be obtained with git checkout ab5eead39 from the main branch. The models were run on 720 processors (15 nodes) on Stampede2 (TACC) through XSEDE allocation TG-EAR180001. Instructions for compiling ASPECT on

Stampede2 can be found at https://github.com/geodynamics/aspect/wiki/Compiling-and-Running-ASPECT-on-TACC-Stampede2.

Fault extraction workflow

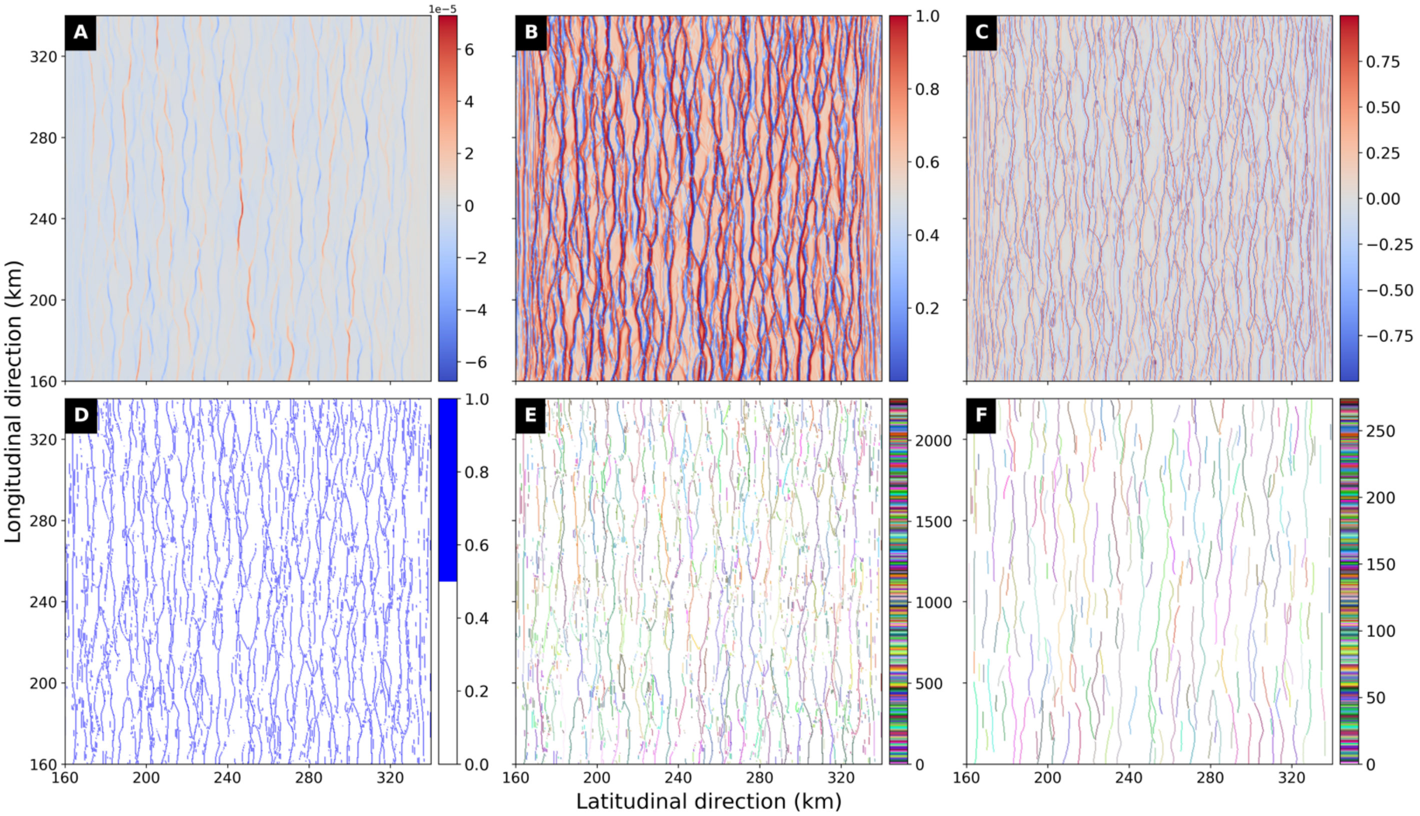

Supplemental Figure 2. Workflow for fault extraction, performed at 5 km depth. The outcome of workflow produces fault labels (**F**) from which key geometric fault properties can be extracted, such as fault length, strain, strike and dip.

The input image can be a depth slice of any field documenting strain (e.g., the finite plastic strain, strain rate invariant, or components of the velocity vector). Our results use $\frac{\partial v_z}{\partial x}$ as the input image (A; Supplementary Fig. 2) as this reveals the dip direction of active faults. The input slice is derived with respect to depth and histogram equalisation is applied (B) in order to i) allow for areas of lower contrast (i.e., smaller faults) to gain a higher contrast, enabling a comprehensive extraction of the entire fault population; and ii) globally adjust contrast for comparison across multiple timesteps. In effect, this step in the workflow produces a value of 0 on one side of the fault, and a value of 1 on the other side of the fault (B), such that in the presence of bifurcation, fault segments are separated. The localities of fault segments are revealed by computing the difference between large contrasts along the longitudinal direction (C), and a predetermined fraction of this range is used to threshold the image (D). The binary array is labelled according to neighbouring connectivity (i.e., horizontal, vertical and diagonal) of pixels (E) (Dillencourt et al., 1992). Noise is filtered out by removing labelled pixels which are smaller than 20. In the case that branching remains, a post-processing script breaks up any remaining branches by locating euclidean distance transformation anomalies which arise as a result of bifurcation, and use the locality as a mask to split labels into two discrete fault segments.

REFERENCES

1. Chapman, D.S., 1986. Thermal gradients in the continental crust. *Geological Society, London, Special Publications*, *24*(1), pp.63-70.
2. Dillencourt, M.B., Samet, H. and Tamminen, M., 1992. A general approach to connected-component labeling for arbitrary image representations. *Journal of the ACM (JACM)*, *39*(2), pp.253-280.
3. Duclaux, G., Huismans, R.S. and May, D.A., 2020. Rotation, narrowing, and preferential reactivation of brittle structures during oblique rifting. *Earth and Planetary Science Letters*, *531*, p.115952.
4. Fraters, M.R., Bangerth, W., Thieulot, C., Glerum, A.C. and Spakman, W., 2019. Efficient and practical Newton solvers for non-linear Stokes systems in geodynamic problems. *Geophysical Journal International*, *218*(2), pp.873-894.
5. Gleason, G.C. and Tullis, J., 1995. A flow law for dislocation creep of quartz aggregates determined with the molten salt cell. *Tectonophysics*, *247*(1-4), pp.1-23.
6. Glerum, A., Thieulot, C., Fraters, M., Blom, C. and Spakman, W., 2018. Nonlinear viscoplasticity in ASPECT: benchmarking and applications to subduction. *Solid Earth*, *9*(2), pp.267-294.

7. Heister, T., Dannberg, J., Gassmöller, R. and Bangerth, W., 2017. High accuracy mantle convection simulation through modern numerical methods–II: realistic models and problems. *Geophysical Journal International*, *210*(2), pp.833-851.
8. Hirth, G. and Kohlstedf, D., 2003. Rheology of the upper mantle and the mantle wedge: A view from the experimentalists. *Geophysical Monograph-American Geophysical Union*, *138*, pp.83-106.
9. Huismans, R.S. and Beaumont, C., 2007. Roles of lithospheric strain softening and heterogeneity in determining the geometry of rifts and continental margins. *Geological Society, London, Special Publications*, *282*(1), pp.111-138.
10. Kronbichler, M., Heister, T. and Bangerth, W., 2012. High accuracy mantle convection simulation through modern numerical methods. *Geophysical Journal International*, *191*(1), pp.12-29.
11. Lavier, L.L., Buck, W.R. and Poliakov, A.N., 2000. Factors controlling normal fault offset in an ideal brittle layer. *Journal of Geophysical Research: Solid Earth*, *105*(B10), pp.23431-23442.
12. Naliboff, J.B., Glerum, A., Brune, S., Péron-Pinvidic, G. and Wrona, T., 2020. Development of 3-D rift heterogeneity through fault network evolution. *Geophysical Research Letters*, *47*(13), p.e2019GL086611.
13. Rose, I., Buffett, B. and Heister, T., 2017. Stability and accuracy of free surface time integration in viscous flows. *Physics of the Earth and Planetary Interiors*, *262*, pp.90-100.
14. Rybacki, E., Gottschalk, M., Wirth, R. and Dresen, G., 2006. Influence of water fugacity and activation volume on the flow properties of fine-grained anorthite aggregates. *Journal of Geophysical Research: Solid Earth*, *111*(B3).
15. Thieulot, C., 2011. FANTOM: Two-and three-dimensional numerical modelling of creeping flows for the solution of geological problems. *Physics of the Earth and Planetary Interiors*, *188*(1-2), pp.47-68.